



HAL
open science

Single myelin fiber imaging in living rodents without labeling by deep optical coherence microscopy.

Juliette Ben Arous, Jonas Binding, Jean-Francois Léger, Mariano Casado, Piotr Topilko, Sylvain Gigan, A. Claude Boccara, Laurent Bourdieu

► **To cite this version:**

Juliette Ben Arous, Jonas Binding, Jean-Francois Léger, Mariano Casado, Piotr Topilko, et al.. Single myelin fiber imaging in living rodents without labeling by deep optical coherence microscopy.. *Journal of Biomedical Optics*, 2011, 16 (11), pp.116012. 10.1117/1.3650770 . hal-00599038

HAL Id: hal-00599038

<https://hal.science/hal-00599038>

Submitted on 8 Jun 2011

HAL is a multi-disciplinary open access archive for the deposit and dissemination of scientific research documents, whether they are published or not. The documents may come from teaching and research institutions in France or abroad, or from public or private research centers.

L'archive ouverte pluridisciplinaire **HAL**, est destinée au dépôt et à la diffusion de documents scientifiques de niveau recherche, publiés ou non, émanant des établissements d'enseignement et de recherche français ou étrangers, des laboratoires publics ou privés.

**Single myelin fiber imaging in living rodents without labeling
by deep-OCM**

Juliette Ben Arous^{a,*}, Jonas Binding^{a,b,c,d,*}, Jean-François Léger^a, Mariano Casado^a, Piotr Topilko^a, Sylvain Gigan^b, A. Claude Boccara^b, Laurent Bourdieu^{a,#}.

a. IBENS, UMR 8197 CNRS and INSERM, ENS, 46 rue d'Ulm, 75005 Paris, France.

b. Institut Langevin, UMR7587 CNRS, ESPCI, 10 rue Vauquelin 75005 Paris, France.

c. Max Planck Institute for Medical Research, Jahnstraße 29, 69120 Heidelberg, Germany.

d. Fondation Pierre-Gilles de Gennes pour la Recherche, 29 rue d'Ulm, 75005 Paris, France

* These authors contributed equally to this work.

Corresponding author,

Juliette Ben Arous : Tel : 33 0144323734; Fax : 33 0144323887; email : juliette.ben.arous@gmail.com

Jonas Binding : Tel : 33 0140794583; Fax : 33 0140794537; email : jonas.binding@espci.fr

Jean-François Léger : Tel : 33 0144323734; Fax : 33 0144323887; email : leger@biologie.ens.fr

Mariano Casado: Tel : 33 01443233752; Fax : 33 0144323887; email : casado@biologie.ens.fr

Piotr Topilko : Tel : 33 01443233984 ; Fax : 33 01443233988; email : piotr.topilko@ens.fr

Sylvain Gigan : Tel : 33 0140794590; Fax : 33 0140794537; email : sylvain.gigan@espci.fr

A. Claude Boccara : Tel : 33 0140794603; Fax : 33 0140794537; email : claude.boccara@espci.fr

Laurent Bourdieu : Tel : 33 0144323734; Fax : 33 0144323887; email : laurent.bourdieu@ens.fr

ABSTRACT

Myelin sheath disruption is responsible for multiple neuropathies in the central and peripheral nervous system. Myelin imaging has thus become an important diagnosis tool. However, *in vivo* imaging has been limited to either low-resolution techniques unable to resolve individual fibers or to low-penetration imaging of single fibers, which can't provide quantitative information about large volumes of tissue, as required for diagnostic purposes. Here, we perform myelin imaging without labeling and at micron-scale resolution with more than 300 μ m penetration depth on living rodents. This was achieved with a prototype (termed 'deep-OCM') of a high-numerical aperture infrared full-field optical coherence microscope, which includes aberration correction for the compensation of refractive index mismatch and high framerate interferometric measurements. We were able to measure the density of individual myelinated fibers in the rat cortex over a large volume of gray matter. In the peripheral nervous system, deep-OCM allows, after minor surgery, in-situ imaging of single myelinated fibers over a large fraction of the sciatic nerve. This allows quantitative comparison of normal and *Krox20* mutant mice, in which myelination in the peripheral nervous system is impaired. This opens promising perspectives for myelin chronic imaging in demyelinating diseases and for minimally invasive medical diagnosis.

KEYWORDS

Myelin, full-field optical coherence tomography, endogenous contrast, optical aberration, live imaging

1) INTRODUCTION

The myelin sheath is an essential component of the vertebrate nervous system composed of glial membrane layers tightly wrapped around axonal fibers. Its high lipid content allows electrical insulation of the axonal membrane and enables saltatory conduction over long distances ensuring rapid, reliable and energetically efficient conduction of action potentials. Disruption of the myelin sheath is involved in central nervous system pathologies such as multiple sclerosis and leukodystrophies and peripheral nervous system (PNS) neuropathies such as Charcot-Marie-Tooth disease (1-2).

Quantitative myelin imaging is a necessary tool to follow demyelination or to evaluate eventual remyelinating treatments. Myelin in the white matter can be visualized *in vitro* and *in vivo* with magnetic resonance imaging, positron emission tomography and near-infrared imaging with a 0.1 to 1 millimeter resolution (3-6). This resolution is insufficient to detect single myelinated axons, thus preventing the study of demyelination in gray matter, where myelinated fibers are sparsely organized. However demyelinating lesions in the gray matter are known to be an important hallmark of pathologies like multiple sclerosis (7).

Different approaches have been recently designed to overcome this limitation. Coherent Anti-stokes Raman Scattering microscopy allows the visualization of single fibers without exogenous labeling (8-9). This technique has a penetration depth of only a few tens of micrometers and cannot provide quantitative information on large volumes of nervous tissue. Third Harmonic Generation provides signals from myelin (10) with an improved penetration but is still a costly and complicated technique and its use for *in vivo* recording in the cortex has not yet been demonstrated. A non invasive method allowing imaging of myelin with individual fiber resolution is therefore still lacking.

Optical coherence tomography (OCT) is a simple yet powerful technique based on interference that allows non-invasive imaging of biological samples and provides optical

sectioning deep into scattering tissues (11-12). Full-field OCT (ff-OCT) is a high spatial resolution version of OCT, the only providing micron resolution in 3D (13). OCT uses the backscattered light due to refractive index (n) variations in the sample as a source of endogenous contrast. The lipid-rich myelin sheath has a high refractive index ($n \sim 1.44$) and lies in an aqueous background ($n \sim 1.33$). Here we show that myelin produces a strong endogenous backscattering signal. To take advantage of this signal, we have designed a prototype of a high-numerical aperture infrared ff-OCT microscope with automatic correction of defocus aberration (14-15). This prototype, designated as deep-OCM, allows high resolution myelin imaging deep in tissue without staining. We present two applications of myelin imaging in large volumes of tissue with single fiber resolution: the myelination of individual fibers during development in the rat cortex and the comparison of sciatic nerve structure in wild type and mutant mice in which myelination in the PNS is impaired.

2) MATERIALS AND METHODS

2.1) Animals.

All animal manipulation and surgical procedures were in accordance with the European Community guidelines on the care and use of animals (86/609/CEE, CE official journal L358, 18th December 1986), French legislation (décret no. 97/748, 19th October 1987, J. O. République française, 20th October 1987), and the recommendations of the CNRS. Male Wistar rats, female Swiss CNP-EGFP mice (16) (CNP: cyclic nucleotide phosphodiesterase, 4 months old), C57BL/6/DBA2 wild type and *Krox20*^{-/-} mice were used in this study (17-18).

2.2) Slice preparation.

For *in vivo* fixation, animals were deeply anesthetized with urethane and perfused transcardially with cold phosphate buffer solution (PBS) followed by 4% paraformaldehyde in PBS solution. In the somato-sensory cortex of rats (P19 and P85) and CNP-EGFP mice, 100 μ m thick slices were cut tangentially to the flattened cortical surface. In the cerebellum of a P19 rat, 300 μ m thick sagittal slices were cut. All slices were stored in PBS before imaging. For myelin immuno-fluorescence labeling, after bleaching (10% H₂O₂, 13.3% DMSO, 53.3% methanol), cortical slices were incubated with rat monoclonal anti-MBP (Myelin Basic Protein) antibodies (1:100, Millipore Bioscience research) followed by goat anti rat Cy3 secondary antibodies (1:500, Jackson Immuno Research). All fluorescence images were acquired using a Leica SP2 confocal microscope with a 10x objective.

2.3) Sciatic nerve preparation.

For *in vitro* imaging, the sciatic nerves of two mice (wild type and *Krox20*^{-/-} mutant, P14) were extracted and laid on glass slides in PBS for immediate imaging. The nerves were not held by a coverslip to prevent them from being crushed. For *in vivo* imaging, a wild type mouse (2 months old) was anesthetized with ketamine (100mg/kg) and xylazine (10mg/kg). A small incision was performed in the left hind limb and the sciatic nerve was exposed. A plastic holder was slipped under the nerve to maintain it and prevent movements. Imaging was performed in PBS without coverslip.

2.4) Surgical procedure for *in vivo* cortex imaging.

Three 3 week old (P20-21; weight ~80g), three 6 week old (P45-46; weight ~250g) and two 12 week old (P86-87; weight ~400g) male Wistar rats were used for *in vivo* somato-sensory cortex imaging. Rats were anesthetized by urethane injection (1.5 g/kg).

Supplementary doses of urethane were applied when necessary. The body temperature of the animal was held at 38°C on a heating blanket during the whole experiment. Animals were maintained in a stereotaxic frame during the surgical procedure. A craniotomy (~3mm in diameter) centered on the somato-sensory cortex was performed on the rat's left hemisphere. In some cases, the dura mater was removed, as indicated in the figure legends. The craniotomy was sealed with a cover slip with 5mm diameter which was glued onto the thinned skull to be in close contact with the brain, in order to prevent brain movements during the imaging procedure. For ff-OCT imaging, the animal was maintained with a metal holder glued on its skull to ensure optical stability. At the end of the experiments, rats were injected with a lethal dose of urethane.

2.5) Deep-OCM set-up.

The microscope (Fig. 1(a)) consists of a low spatial and temporal coherence light source (250 W halogen lamp) with the standard Köhler microscope illumination, a Linnik interferometer (i.e. a Michelson interferometer with an objective in each arm), a tube lens and a camera. The water immersion objectives used were either Zeiss IR-Achroplan 40x/0.8 W or Olympus UMPlanF 10x/0.3 W. For dispersion correction, a coverslip identical to the one used to cover the sample was placed in the reference arm. To avoid the back-reflection from the coverslip on the camera, the former was slightly tilted. A 50 cm doublet was used as a tube lens to image the sample and the reference arm mirror onto the camera. Two different cameras were used: an infrared InGaAs camera (Xeva-1.7-320, Xenics Infrared Solutions, Leuven, Belgium) and a silicon camera (Pantera 1M60, Dalsa, Waterloo, Canada). Myelin fibers were detected with both sensors. Deep-OCM images taken with the InGaAs camera are noted as “IR” in the text, whereas images from the silicon camera are described as “deep-red”. The InGaAs sensor chip had 320x256 pixels (pixel size: 30µm) and the silicon chip had

1024x1024 pixels (pixel size: 12 μm). They were operated at 66Hz and 57Hz respectively, triggered by a NI 6722 digital I/O board (National Instruments, Austin, Texas) controlled by the software Light-CT (LLTech, Paris). A synchronized rectangular 33 or 28.5 Hz signal drove the Piezo Linear Stage Actuator (PI P-753.11C, Physik Instrumente GmbH, Karlsruhe) onto which the reference arm mirror was mounted. The piezo actuator amplitude was adapted to produce a change in reference arm length of $\lambda/2$, so that the relative phase between both arms of the interferometer would change by π . Taking the difference of subsequent camera images would therefore separate the interference signal from the background light, implementing a two-step phase stepping protocol. The software light-CT (LLTech Inc.) running on a standard PC allowed real-time display of the infrared images at 33 Hz, while the higher pixel number of the silicon camera limited display speed to about 15 Hz. Both the sample z position and the relative arm length could be changed with two motorized linear stages (M-VP-25XA, Newport).

With this setup the axial resolution (sectioning ability) is mainly due to the coherence length of the source whereas the lateral resolution is due to the numerical aperture of the microscope objectives. In the lowest resolution configuration, with 10x objectives and the InGaAs camera (peak of the effective spectrum: $\lambda_{\text{max}}=1100\text{nm}$), the lateral sampling of the system was $1.07\mu\text{m}$, the lateral resolution $2.2\mu\text{m}$ (calculated using the Rayleigh formula $0.6*\lambda_{\text{max}}/\text{NA}$, where NA is the objective numerical aperture), and the axial resolution $3.3\mu\text{m}$ (measured as the full width at half maximum of the interferogram). In the highest resolution configuration, with 40x objectives and the silicon camera ($\lambda_{\text{max}}=770\text{nm}$), the lateral sampling of the system was $0.1\mu\text{m}$, the lateral resolution $0.5\mu\text{m}$ and the axial resolution $1.15\mu\text{m}$.

2.6) Automatic compensation of defocus aberration due to refractive index mismatch

Refractive index mismatch between the immersion liquid in the sample arm and the sample causes depth-dependent defocus in ff-OCT (14-15). Refractive index mismatch compensation was performed on-line as described previously (14-15). Briefly, compensation is obtained by keeping the coherence volume at constant depth inside the sample and moving the actual focus into this same position (Fig. 1(b)). Due to the aqueous immersion (group index n_g), a movement l of the sample objective away from the sample increases the (paraxial) optical path in water by $2 \cdot n_g \cdot l$, while the optical path in air only decreases by $2 \cdot l$. To keep the coherence volume at constant depth in the sample, a displacement l of the sample objective should be therefore associated with a displacement $d(l) = \ell(n_g - 1)$ of the reference arm. The metric used to determine the optimal positions l and $d(l)$ was the total image intensity (15).

2.7) Stitching.

For images with a large field of view, a prototype of a ff-OCT microscope from the company LLTech was used. It used a 640x512 pixel InGaAs Xenics Xeva camera, Olympus UPlanF 10x/0.3W objectives and a Märzhäuser xy translation stage. Stitching of individual images with 20% overlap was performed using the ImageJ plugin “Stitch Image Collection” by Stephan Preibisch, Max Planck Institute of Molecular Cell Biology and Genetics in Dresden.

2.8) Quantification

For myelin quantification, vertical stacks of images were acquired in confocal immuno-fluorescence and in deep-OCM (both *in vitro* and *in vivo*). The stacks had a total depth of 60 to 90 μm and were acquired either just below the brain surface (*in vivo*) or in the first tangential slice from the brain surface (*in vitro*). The total length of myelin filaments per

unitary surface was computed as follows. The length of myelin fibers contained within the depth of field in each independent frame was first measured manually using ImageJ. The average and standard error of the mean of fiber length density per unitary surface was then calculated for 23 to 37 frames chosen in at least 4 different stacks in each imaging condition. Images from stacks obtained in rats of a given age were pooled together. Frame sizes were 120 x 120 μm (immuno-fluorescence confocal), 105 x 105 μm (*in vitro* 40X deep-red deep-OCM) and 79 x 63 μm (*in vivo* 40X IR deep-OCM). The volume density of fiber length was obtained from the surface density by taking into account the thickness of each optical section (5.6 μm in confocal microscopy, 1.15 μm in *in vitro* deep-OCM, 3.3 μm in *in vivo* deep-OCM).

Fiber diameters, lengths, and interfringe spacings were determined manually using the ImageJ Plot Profile tool. Fiber inclination A was calculated from the fibers' apparent length L via $\tan(A)=L/l_z$, where l_z is defined as the full width of the interferogram measured at 10% of the maximum ($l_z=2.3 \mu\text{m}$ for 40x deep-red deep-OCM).

Statistical comparisons were performed by standard Student's t-tests.

3) RESULTS

3.1) *Deep-OCM allows in vitro and in vivo imaging of myelinated fibers*

Deep-OCM has the following unique features (Fig. 1(a) and Materials and Methods). It allows either deep-red imaging (wavelength range 700-850 nm, measured at half the peak height) for maximum lateral resolution or near-infrared imaging (wavelength range 1000-1170 nm) to increase further the depth penetration due to decreased scattering at longer wavelengths (19). In all cases, fast (~30Hz) image acquisition is performed to prevent motion artifacts and loss of contrast due to sample motion. The objectives used are either a 10x

objective for the observation of large fields of view or a 40x objective with a numerical aperture (NA) of 0.8 to maximize lateral resolution. Large NA makes the setup highly sensitive to defocus induced by refractive index mismatch between immersion medium and tissue (14-15). Refraction at the brain surface indeed causes the actual focus z_A of the objective to be shifted deeper into the sample with respect to the nominal focus z_N (Fig. 1(b)) whereas the coherence volume penetrates the tissue slower than the nominal focus (Fig. 1(b)) (15). This spatial separation of coherence volume and actual focus results in a loss in OCT signal: even the small refractive index mismatch between immersion water and brain tissue of around 2% is sufficient for depth penetration not to be limited by scattering-induced exponential signal decrease, as expected from Beer-Lambert law, but by signal loss due to defocus (15). We therefore systematically applied automated defocus compensation, increasing the penetration depth by typically a factor of 2.5 (15). In these conditions, deep-OCM provides micrometer resolution in the 3 dimensions and in the depth of the tissue.

3.2) In vitro imaging of individual myelinated fibers.

Using deep-OCM, we were able to observe fibers in the rodent brain tissue. They show up with very high endogenous contrast due to backscattering of the incident light (Fig. 1(b) and 1(c)). Compensation of index-mismatch-induced defocus was mandatory to observe the fibers with high contrast and resolution (Fig. 1(b)). In 40x deep-red images of rat cortical slices (Fig. 1(c)), the observed diameter of the fibers was $0.6 \pm 0.1 \mu\text{m}$ and was therefore at the diffraction limit (microscope lateral resolution: $0.56 \mu\text{m}$), in good agreement with the diameter of individual myelinated fibers in the rat brain (20). Note that these fibers appear discontinuous in the images, because of the presence of interference fringes on their reflective surface. The fringe spacing along the fibers allows the quantitative determination of the fiber inclination (Fig. 2).

To confirm that the observed fibers were myelinated axons, we compared deep-OCM and confocal fluorescence images of fiber bundles in the same slice of the corpus callosum of a mouse expressing the enhanced green fluorescent protein (EGFP) under the control of the 2'-3'-cyclic nucleotide 3'-phosphodiesterase (CNP) promoter which causes specific labeling of oligodendrocytes. We observed the same myelin bundles in both images, whereas the cellular bodies of oligodendrocytes were only visible in the fluorescence image (Fig. 1(d)).

In order to quantify the proportion of myelinated fibers detected by deep-OCM imaging, 40x deep-red images of a fixed rat horizontal cortical slice (Fig. 3(b)) were compared to confocal images of another cortical slice of the same animal where the myelin basic protein MBP had been immunostained (Fig. 3(a)). This quantization was performed for rats of two different ages (3 and 12 weeks old). The fiber densities measured with the two different methods were not significantly different for 12 week old animals (Student t-test, $P=0.39$ Fig. 3(c)). In the case of 3 week old animals, no fibers were detected by deep-OCM imaging, whereas a very small number could be detected after immunostaining (~ 3% of the fiber density in adults). These few patchy myelinated zones may have been missed due to the smaller field of view of the deep-OCM images. These results indicate that this technique can be used for a quantitative analysis of myelinated axons.

Myelinated fibers could also be detected by deep-OCM in other brain structures over large fields of view. We reconstructed a complete image of a fixed rat cerebellum sagittal slice with micron resolution by stitching consecutive fields of view (10x IR, 8mm x 8mm, Fig. 4(a)). The stereotyped organization of the cerebellar cortex allows unequivocal identification of the different structures. Because of its rich myelin content, the white matter was the most visible structure in the cerebellum. The molecular and granular layers appeared clearly distinct and the Purkinje cell somata were visible as hollow structures (Fig. 4(c)).

Individual myelinated fibers could be readily observed in the cerebellar white matter (Fig. 4(d)), beyond the depth sectioning ability of standard brightfield microscopy.

Myelin imaging was also performed in the Peripheral Nervous System. Deep-OCM 3D reconstruction was used to obtain the structure of an acutely dissected mouse sciatic nerve *in vitro*, in which individual myelinated fibers could be discriminated (Fig. 5(a), Movie 1). Deep-OCM imaging allows optical reconstruction of a large fraction (about one half) of the whole nerve (Fig. 5(a)) with micrometer resolution. In order to check our ability to evaluate pathological demyelinating situations, we imaged the sciatic nerves of *Krox20* mutant mice. *Krox20* is a transcription factor whose inactivation in Schwann cells results in impaired myelination of the PNS (17-18). We observed a strong difference between nerves of *Krox20* mutant and wild type mice (Fig. 5(b)). Indeed, individual fibers could not be discriminated in mutant animals. Moreover, in identical imaging conditions, the reflected light amplitude was ~40% stronger in wild type nerves than in mutant nerves. Thus, deep-OCM can be used to evaluate pathological myelin alteration in peripheral nerves.

3.3) In vivo imaging of individual myelinated fibers.

We tested whether sciatic nerve deep-OCM imaging could be performed *in vivo* in an anesthetized wild type mouse, using minimal surgery to expose the nerve and stabilize it (Fig. 6(a)). This was necessary to prevent respiratory or heart beat movements. *In vitro* and *in vivo* images were of comparable quality (Fig. 6(b) vs. Fig. 5(a)).

Finally, we performed *in vivo* deep-OCM myelin imaging in the somato-sensory cortex of anesthetized rats. The animals were maintained in the imaging system by a tight head fixation to prevent movement during image acquisition (Fig. 7(a)). The use of IR imaging and of refractive index-mismatch correction are particularly important in deep *in vivo* imaging where they improve considerably the contrast and resolution of images. Two

configurations were tested. In the first situation, the dura was removed, which potentially increases brain motion artifacts. In the second situation, the dura was preserved, despite its large backscattering. Detection of myelin fibers in the rat cortex was possible in both conditions (Fig. 7(b) and Fig. 7(c)).

Using deep-OCM, we followed the developmental profile of myelinated fibers from 3 to 12 weeks (Fig. 7(c) and Fig. 7(d)). Myelinated axons were observed *in vivo* up to 350 μ m deep into the somato-sensory cortex of 6 and 12 week old animals (Fig. 7(c), middle and right), whereas no fibers were observed in the cortex of 3 week old animals (Fig. 7(c), left). The density of fibers in the first 150 μ m below the brain surface was consistent with the one measured *in vitro* (Fig. 7(d) and Fig. 3). It was similarly high for 6 and 12 week old rats (Student t-test, $P=0.42$, Fig. 7(d)), and was reduced in both cases at levels deeper than 150 μ m, in good agreement with previous histological studies ((21-22) and <http://brainmaps.org>).

4) DISCUSSION

In this study we have shown that deep-OCM allows quantitative imaging of individual myelinated fibers *in vitro* and *in vivo* in the rodent nervous system, with micron-size resolution, without labeling and over large volumes of tissue, up to 350 μ m deep into the tissue. Deep-OCM combines several technical advances compared to standard ff-OCT microscopy, such as fast acquisition rate, IR imaging, large numerical aperture microscope objectives and real time defocus correction (14-15, 19). Deep-OCM imaging of myelinated fibers benefits from their large backscattered signal. This may arise from the high local refractive index of fibers due to their high lipid content. However, whereas imaging at moderate depth was possible in a standard configuration using deep-red light, imaging at greater depth was only possible by combining infrared detection with the correction of

defocus aberration due to refractive index mismatch between immersion medium and brain tissue. Without defocus correction, both signal strength and resolution quickly degrade with depth. Finally, imaging at high temporal resolution with fast cameras in addition to a tight tissue mechanical fixation was required to avoid motion artifacts due to breathing or heart beat.

In the PNS, fast image acquisition of the myelin structure of sciatic nerves at high resolution was achieved both *in vitro* and *in vivo*, and defects of the myelin sheath observed in the raw images could be easily quantified from the reflected amplitude. As the access to the peripheral nervous system is quite simple and requires only minor surgery, this method may be used, in the future, in human patients with peripheral neuropathies. Deep-OCM-based myelin imaging of the sciatic nerve could replace nerve biopsy, which is a standard procedure for diagnosing certain neuropathies. It could thereby help avoid neuropathic side effects associated to nerve biopsies.

Deep-OCM also allowed us to record images of individual myelinated fibers *in vivo* within the somato-sensory cortex of anesthetized rats, without exogenous labeling, and either when the dura matter was removed or directly below the intact dura mater. Quantification of myelinated fiber density was obtained from the image analysis. Similar axonal densities have been measured in the superficial layers of the rat cortex (23). By this approach, we could observe the developmental appearance of myelin structures in the adult rat brain. Compared to other techniques that work in this resolution and penetration depth regime, such as two-photon microscopy of genetically labeled oligodendrocytes, deep-OCM has the advantage that it images directly the local increase of refractive index caused by the high lipid content of the myelin sheath. This should allow extensive and even chronic imaging without the risk of signal deterioration due to bleaching, as would be the case in two-photon microscopy. Such chronic imaging of individual myelinated fibers in the upper layers of the rat cortex, which

are not visible in whole-brain imaging techniques such as MRI due to the limited resolution, could be of considerable interest in neuropathies progression studies. Our observations open perspectives of application to chronic experiments in rodents, notably for the longitudinal study of cortical demyelination and remyelination. To our knowledge, no other existing technique gives access to this information.

In conclusion, deep-OCM makes a fine-scale analysis of myelination processes possible, both in the cerebral cortex and in the peripheral nervous system. Such analysis currently requires time-consuming and invasive histological methods. Our technique is relatively non-invasive, affordable and fast, and provides real time imaging without complex off-line image treatment. It opens promising possibilities for *in vivo* acute or chronic myelin imaging as well as for the diagnosis of myelin pathologies.

Acknowledgements

We would like to thank Marie-Stéphane Aigrot, Bruno Stankoff and Catherine Lubetzki for their helpful comments. We thank them also for transferring the transgenic CNP-GFP mice and Vittorio Gallo for authorizing us to use them. We would also like to thank Charles Brossollet, Benjamin Mathieu, and Gaspard Gerschenfeld for their help and Shawn Mikula for critical discussions. This work was supported by ANR RIB grants MICADO ANR-07-RIB-010-02 and ANR-07-RIB-010-04. J.B. was funded by a PhD fellowship from Fondation Pierre-Gilles de Gennes.

References

1. S. S. Scherer and L. Wrabetz, "Molecular mechanisms of inherited demyelinating neuropathies," *Glia* 56(14), 1578-1589 (2008)
2. N. Baumann and D. Pham-Dinh, "Biology of oligodendrocyte and myelin in the mammalian central nervous system," *Physiol Rev* 81(2), 871-927 (2001)
3. C. Laule, I. M. Vavasour, S. H. Kolind, D. K. Li, T. L. Traboulsee, G. R. Moore and A. L. MacKay, "Magnetic resonance imaging of myelin," *Neurotherapeutics* 4(3), 460-484 (2007)
4. S. Mori and J. Zhang, "Principles of diffusion tensor imaging and its applications to basic neuroscience research," *Neuron* 51(5), 527-539 (2006)
5. B. Stankoff, Y. Wang, M. Bottlaender, M. S. Aigrot, F. Dolle, C. Wu, D. Feinstein, G. F. Huang, F. Semah, C. A. Mathis, W. Klunk, R. M. Gould, C. Lubetzki and B. Zalc, "Imaging of CNS myelin by positron-emission tomography," *Proc Natl Acad Sci U S A* 103(24), 9304-9309 (2006)
6. C. Wang, C. Wu, D. C. Popescu, J. Zhu, W. B. Macklin, R. H. Miller and Y. Wang, "Longitudinal near-infrared imaging of myelination," *J Neurosci* 31(7), 2382-2390 (2011)
7. J. J. Geurts, S. D. Roosendaal, M. Calabrese, O. Ciccarelli, F. Agosta, D. T. Chard, A. Gass, E. Huerga, B. Moraal, D. Pareto, M. A. Rocca, M. P. Wattjes, T. A. Yousry, B. M. Uitdehaag and F. Barkhof, "Consensus recommendations for MS cortical lesion scoring using double inversion recovery MRI," *Neurology* 76(5), 418-424 (2011)
8. Y. Fu, T. B. Huff, H. W. Wang, H. Wang and J. X. Cheng, "Ex vivo and in vivo imaging of myelin fibers in mouse brain by coherent anti-Stokes Raman scattering microscopy," *Opt Express* 16(24), 19396-19409 (2008)
9. J. Imitola, D. Cote, S. Rasmussen, X. S. Xie, Y. Liu, T. Chitnis, R. L. Sidman, C. P. Lin and S. J. Khoury, "Multimodal coherent anti-Stokes Raman scattering microscopy reveals

microglia-associated myelin and axonal dysfunction in multiple sclerosis-like lesions in mice," *J Biomed Opt* 16(2), 021109 (2011)

10. M. J. Farrar, F. W. Wise, J. R. Fetcho and C. B. Schaffer, "In Vivo Imaging of Myelin in the Vertebrate Central Nervous System Using Third Harmonic Generation Microscopy," *Biophys J* 100(1362-1371) (2011)

11. J. G. Fujimoto, "Optical coherence tomography for ultrahigh resolution in vivo imaging," *Nat Biotechnol* 21(11), 1361-1367 (2003)

12. J. G. Fujimoto, M. E. Brezinski, G. J. Tearney, S. A. Boppart, B. Bouma, M. R. Hee, J. F. Southern and E. A. Swanson, "Optical biopsy and imaging using optical coherence tomography," *Nat Med* 1(9), 970-972 (1995)

13. L. Vabre, A. Dubois and A. C. Boccara, "Thermal-light full-field optical coherence tomography," *Opt Lett* 27(7), 530-532 (2002)

14. S. Labiau, G. David, S. Gigan and A. C. Boccara, "Defocus test and defocus correction in full-field optical coherence tomography," *Opt Lett* 34(10), 1576-1578 (2009)

15. J. Binding, J. Ben Arous, J.-F. Léger, S. Gigan, C. Boccara and L. Bourdieu, "Brain refractive index measured in vivo with high-NA defocus-corrected full-field OCT and consequences on two-photon microscopy," *Opt Express* 19(6), 4833-4847 (2011)

16. X. Yuan, R. Chittajallu, S. Belachew, S. Anderson, C. J. McBain and V. Gallo, "Expression of the green fluorescent protein in the oligodendrocyte lineage: a transgenic mouse for developmental and physiological studies," *J Neurosci Res* 70(4), 529-545 (2002)

17. P. Topilko, S. Schneider-Maunoury, G. Levi, A. Baron-Van Evercooren, A. B. Chennoufi, T. Seitanidou, C. Babinet and P. Charnay, "Krox-20 controls myelination in the peripheral nervous system," *Nature* 371(6500), 796-799 (1994)

18. F. Couplier, L. Decker, B. Funalot, J.-M. Vallat, F. Garcia-Bragado, P. Charnay and P. Topilko, "CNS/PNS boundary transgression by central glia in the absence of Schwann cells or Krox20/Egr2 function," *J Neurosci* 30(17), 5958-5967 (2010)
19. D. Sacchet, J. Moreau, P. Georges and A. Dubois, "Simultaneous dual-band ultra-high resolution full-field optical coherence tomography," *Opt Express* 16(24), 19434-19446 (2008)
20. G. Partadiredja, R. Miller and D. E. Oorschot, "The number, size, and type of axons in rat subcortical white matter on left and right sides: a stereological, ultrastructural study," *J Neurocytol* 32(9), 1165-1179 (2003)
21. S. Mikula, I. Trotts, J. M. Stone and E. G. Jones, "Internet-enabled high-resolution brain mapping and virtual microscopy," *Neuroimage* 35(1), 9-15 (2007)
22. I. Trotts, S. Mikula and E. G. Jones, "Interactive visualization of multiresolution image stacks in 3D," *Neuroimage* 35(3), 1038-1043 (2007)
23. J. T. Eayrs and B. Goodhead, "Postnatal development of the cerebral cortex in the rat," *J Anat* 93(385-402 (1959)

FIGURE LEGENDS

Figure 1. Deep-OCM myelin imaging. (a) Deep-OCM setup incorporating IR and deep-red illumination, high NA objectives, compensation for defocus due refractive index mismatch and high speed camera. (b) Impact of index mismatch correction for OCT imaging in brain tissues. Left: In an index-matched sample, focus and coherence volume would coincide at the nominal focus (NF). Refractive index mismatch shifts the actual focus (AF) and the coherence volume (CV) away from NF so that ff-OCT images are blurred. Right: After correction, AF and CV coincide, which provides high resolution and highly-contrasted images. The images shown below the schemes are 40x IR deep-OCM *in vivo* images of myelin fibers in the

somato-sensory cortex of a 6 week old rat ($z=120\mu\text{m}$ below the surface of the tissue, after removal of the dura). Left: uncorrected image; right: corrected image, defocus correction $d=6.5\mu\text{m}$, with the same exposure time. (c) Maximum projection of 40x deep-red deep-OCM image stack in a cortex slice ($z=250\mu\text{m}$ below the brain surface) (d) Comparison of confocal fluorescence images (left) and stitched 10x IR deep-OCM images (right) of the same slice of corpus callosum of a CNP-EGFP mouse. CNP-EGFP is expressed specifically in oligodendrocytes. In CNP-EGFP fluorescence images, the oligodendrocytes' cellular bodies and the myelin sheath are visible, whereas only myelin appears in deep-OCM images.

Figure 2. Interferometric measurement of the inclination of myelinated fibers. (a-b) In deep-OCM images, the visible length L of the fiber within the coherence-gated optical section corresponds to an inclination A of the fiber, and therefore to a fringe spacing I on the camera. (c) In 40x deep-red deep-OCM images in the white matter of cerebellum slices, the inclination of fibers A calculated from the measurement of their visible length L (see Materials and Methods) corresponds to the theoretically predicted angle for a given fringe spacing I . Measuring the fringe spacing on a fiber in a 2D image therefore provides an estimate of its inclination with respect to the optical axis.

Figure 3. *In vitro* deep-OCM imaging and quantification in the rat somato-sensory cortex. (a) Maximum projection of 10x confocal immuno-fluorescence images (anti-MBP, myelin basic protein) of tangential slices of rat somato-sensory cortex ($1\text{mm} \times 1\text{mm} \times 60\mu\text{m}$, $z=150\mu\text{m}$ below the brain surface) from a P19 and a P85 rat. (b) Maximum projections of 40x deep-red deep-OCM image stacks in adjacent cortex slices ($z=250\mu\text{m}$) from the same animal ($70\mu\text{m} \times 90\mu\text{m} \times 60\mu\text{m}$) as in (A). (c) Fiber length density (unit: $\text{mm of fiber}/\text{mm}^3$ of tissue) measured *in vitro* in tangential slices of rat somato-sensory cortex, by 40x deep-red deep-

OCM and by confocal immuno-fluorescence, for 3 week old and 12 week old animals. Error bars are the standard error of the mean.

Figure 4. High resolution deep-OCM imaging of rat cerebellar slices. (a) Stitched 10x IR deep-OCM image of a fixed sagittal slice of a 3 week old rat. (b) Brightfield low resolution image with indication of the different cerebellar lobules. (c) Detail of the 3 regions delimited in A. WM: white matter; GCL: granule cell layer; PCL: Purkinje cell layer; ML: molecular layer. (d) 40x deep-red deep-OCM images of cerebellar white matter.

Figure 5. *In vitro* mouse sciatic nerve imaging. (a) Stitched 10x IR deep-OCM images of an acute mouse sciatic nerve. Maximum projection of a vertical stack (total depth: 200 μ m); the bright central zone corresponds to a strong reflection on the upper surface of the nerve. Insert, from left to right: x-z reslice of the stack and individual images 25 μ m, 50 μ m and 75 μ m deep into the nerve. (b) Comparison of a wild type mouse nerve (left) and a Krox20^{-/-} mutant nerve (right). In both cases, maximum projection of a vertical stack of 10x IR deep-OCM images (total depth: 200 μ m).

Figure 6. *In vivo* deep-OCM myelin imaging in the mouse sciatic nerve. (a) Animal preparation. (b) *In vivo* 10x IR deep-OCM image of the sciatic nerve of a wild type mouse (z=50 μ m below the surface).

Figure 7. *In vivo* deep-OCM myelin imaging in the rat somato-sensory cortex. (a) Animal and brain stabilization. (b) *In vivo* 10x IR deep-OCM images of the somato-sensory cortex of a 6 week old rat, under the intact dura mater. Maximum projection of a vertical stack of images starting at 120 μ m and ending at 140 μ m below the brain surface. (c) *In vivo* 40x IR

deep-OCM images of the somato-sensory cortex of 3 week old (left, $z=120\mu\text{m}$), 6 week old (middle, $z=120\mu\text{m}$) and 12 week old (right, $z=150\mu\text{m}$) rats (dura mater was removed in all three cases). (d) Developmental profile of the fiber length density (unit: mm of fiber/ mm^3 of tissue) in the cortex. Error bars are the standard error of the mean.

Movie 1. *In vitro* 10x IR deep-OCM imaging of an acute mouse sciatic nerve. 3D reconstruction from a $200\mu\text{m}$ vertical stack with $0.4\mu\text{m}$ step. The field of view is $345\mu\text{m} \times 276\mu\text{m}$.

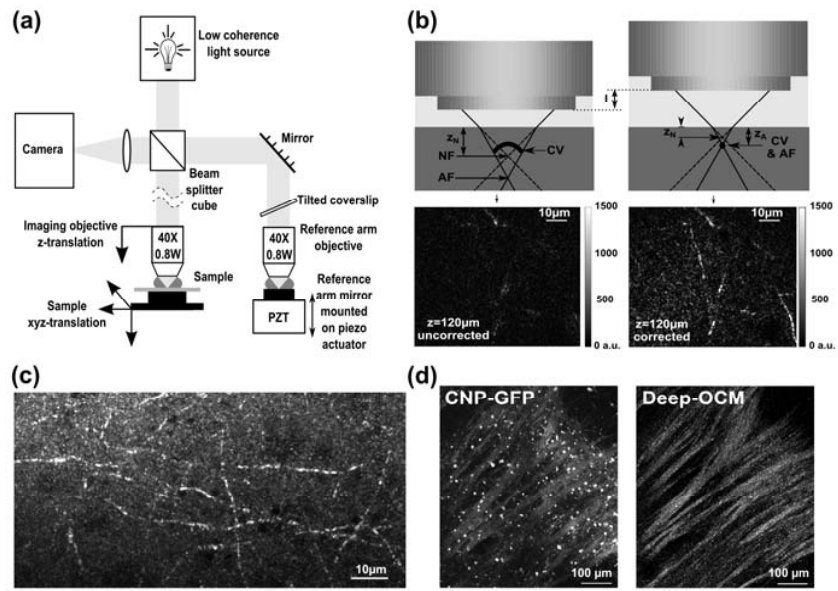


Figure 1

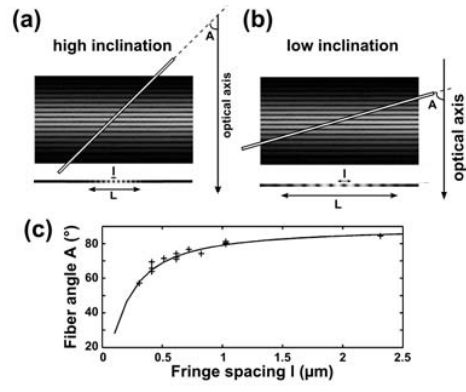


Figure 2

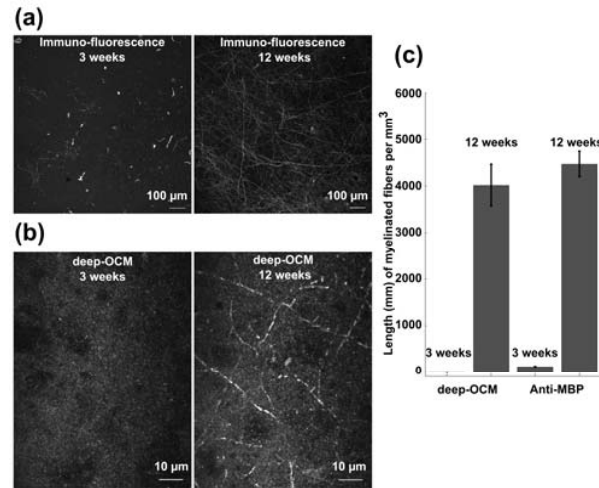


Figure 3

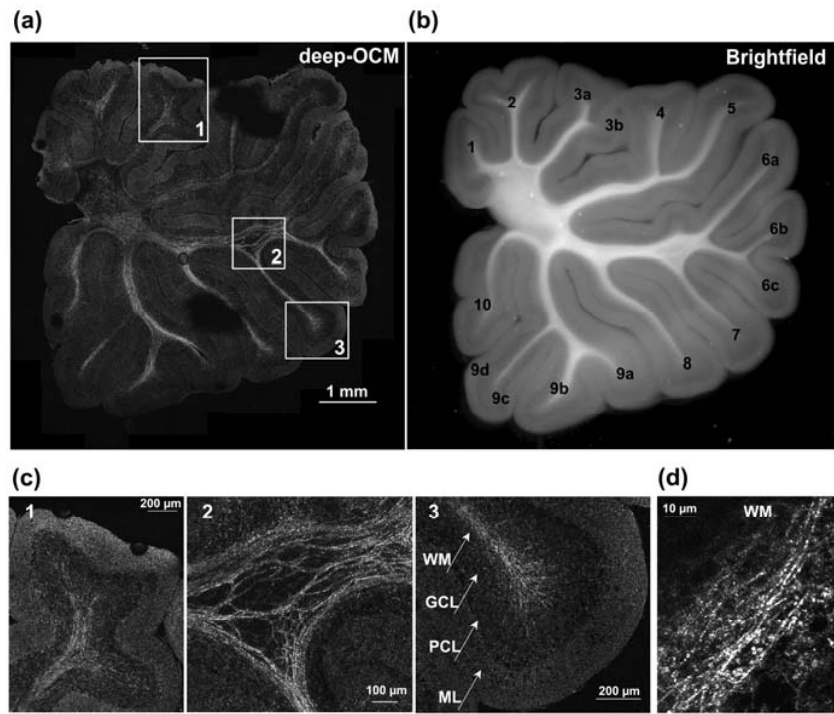


Figure 4

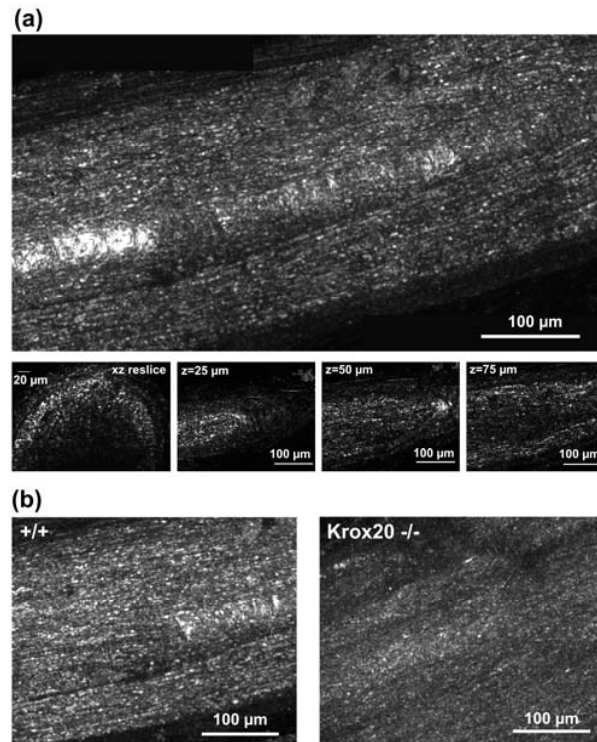


Figure 5

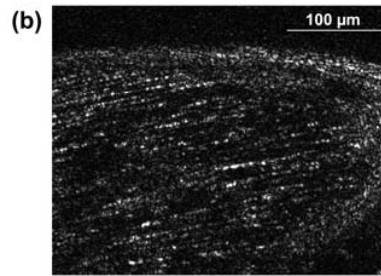
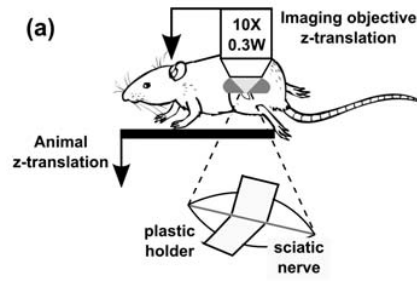


Figure 6

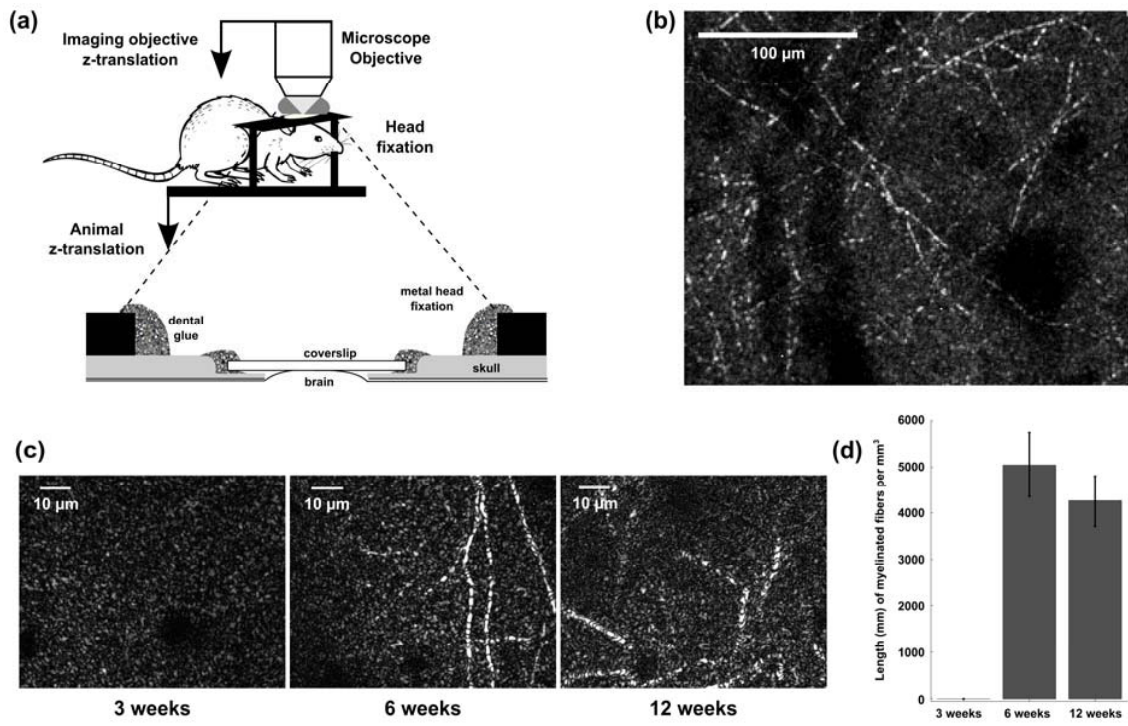


Figure 7